CHAPTER 6
TLD EXPERIMENTS

It is a capital mistake to theorize before you have all the evidence...
It biases the judgment
-Sherlock Holmes (Sir Arthur Conan Doyle)

The sloshing-slamming analogy and impact characteristics for modeling Tuned Liquid Dampers (TLDs) were introduced in chapter 2. This chapter focusses on experimental studies conducted on TLDs. Shaking table experiments are conducted to obtain the parameters needed to model the impact characteristics introduced in chapter 2. Impact pressures due to sloshing are also measured along the height of the container wall. This helps to glean better understanding regarding the nature of sloshing-slamming noted at large amplitudes of excitation. Finally, an innovative technique known as *Hardware-in-the-loop* is utilized to conduct structure-damper interaction experiments.

6.1 Introduction

Sloshing of liquids has prompted numerous experimental studies in various disciplines due to the complexity of the problem and the difficulty in developing an analytical model. Some of the relevant work done in the area of liquid dampers is briefly reported here. The earliest experimental studies on TLDs are reported by Modi and Welt, 1987 and Fujino *et al.* 1988. A series of experimental studies, summarized in Modi *et al.* 1995, were conducted using *nutation dampers*. These dampers covered different geometries like a toroidal ring, rectangular or circular cross-section cylinders, and in some situations may include baffles, screens, particle suspensions to manage liquid sloshing. Damper charac-

teristics were determined by varying the amplitude and frequency of excitation. Fujino *et al.* 1988 carried out parametric studies of cylindrical containers by free-oscillation experiments. Effects of liquid viscosity, roughness of container bottom, air gap between the liquid and tank roof, and container size on the overall TLD damping were studied.

Experimental studies have been carried out for rectangular TLDs in the region of relatively small to medium vibration amplitudes, where breaking of a wave does not occur, and the results have been found to be in good agreement with analytical results obtained by the shallow water theory (Fujino *et al.* 1992; Sun and Fujino, 1994; Sun *et al.* 1995). Similar experiments were done by Koh *et al.* (1994) who considered earthquake type excitations as opposed to sinusoidal excitations utilized in previous studies. Large amplitude excitations, which are more representative of earthquakes, were also investigated through similar shaking table tests and numerical modeling by Reed *et al.* (1998). Experimental investigations of TLDs with submerged nets and other flow dampening devices were studied by Fediw *et al.* 1993 and Warnitchai and Pinkaew (1998). Chung and Gu, 1999 carried out experimental verification of the performance of TLDs in suppressing vortex-excited vibration on a small-scale structural model in a wind tunnel. Experimental verification of active TLD systems have been conducted by Chang *et al.* 1997 and Natani (1998). A comprehensive review of various analytical and experimental studies for sloshing dynamics is documented in Ibrahim *et al.* 2001.

As mentioned earlier, theoretical analyses are not able to predict sloshing pressures and forces in the neighborhood of resonance for large amplitude excitations. In chapter 2, it was shown that the impact component is an important component of the overall sloshing force. Therefore, experimental studies are conducted to better understand the nature of the liquid impact on the container walls. Previous experimental studies have

been conducted, most notably in ship engineering (Bass *et al.* 1980) and marine engineering applications (Schmidt *et al.* 1992; Hattori *et al*. 1994). However, specific studies of impact pressures and their relation to the TLD performance have not been studied previously. The present chapter presents experimental studies conducted on shallow water TLDs, which shed more light into the nature of sloshing-slamming caused at large amplitude excitations.

6.2 Experimental Studies

In order to derive the impact characteristics of TLDs as discussed in Chapter 2, experiments were conducted on a rectangular TLD, shown in Fig. 6.1(a). The tank had the following dimensions: length a = 25.4 cm, width w = 10.64 cm and a liquid height h = 3 cm.

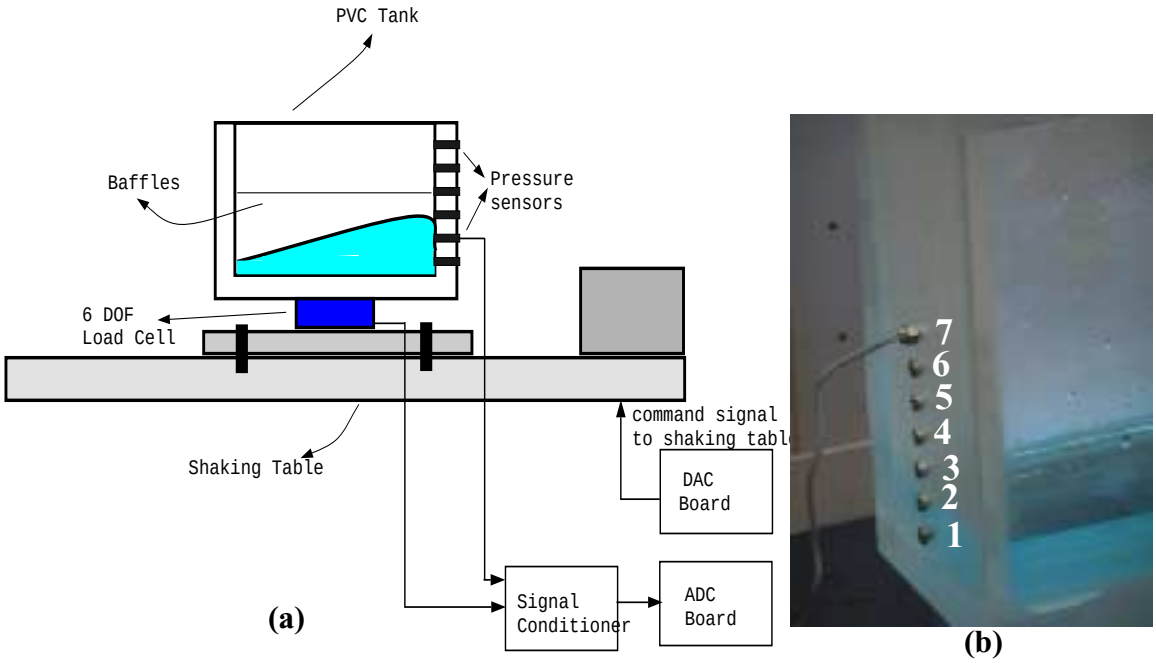

Figure 6.1 (a) Schematic of the experimental setup (b) pressure sensor locations

From the linear wave theory, one can compute the natural frequency of the first sloshing mode as,

$$\omega_f = \frac{1}{2\pi}\sqrt{\frac{g\pi}{a}\tanh\left(\pi\frac{h}{a}\right)} \tag{6.1}$$

Using Eq. 6.1, the first sloshing mode frequency is computed to be 1.05 Hz. The total mass of water is $m = \rho awh$ =0.8 kg. The linear damping is calculated from an expression given in Abramson, 1966:

$$\zeta_f = \sqrt{\frac{\nu_f}{a^{3/2}\sqrt{g}}} \tag{6.2}$$

where ν_f is the kinematic viscosity of water, a is the length of the tank in the direction of the excitation, and g is the gravitational constant. Based on representative values for the parameters in Eq. 6.2, ζ_f was found to be equal to 0.004 (0.4%). The water depth ratio is 0.12 which satisfies the shallow water assumption ($h/a < 0.15$). The excitation amplitudes considered in this study range from 0.1 to 2 cm, which correspond to A_e/a ratio of 0.004 to 0.08. The excitation frequency ratio ($\gamma_f = \omega_e/\omega_f$) in the sine-sweep tests was in the range 0.85-1.3.

A six degree of freedom load cell was utilized to measure the base shear due to liquid sloshing. A calibration matrix was used to determine the net shear force in the x-direction. An accelerometer with a gain equal to the mass of the empty tank estimates the contribution of the inertial component of the shear force due to the empty tank. This was verified in the laboratory by testing the tank without water and comparing the value of the base shear force and the accelerometer reading. The net sloshing force, $F_b(t)$, due to the liquid sloshing alone is obtained by subtracting the inertial contribution of the empty tank from the total shear force. Finally, the shear force was expressed in a non dimensional form as,

$$F_b' = \frac{F_b}{m\omega_e^2 A_e} \tag{6.3}$$

Pressure sensors were also mounted along the wall of the TLD to monitor the impact pressures generated due to the liquid sloshing. The experimental setup is shown in Fig. 6.1(b), wherein seven holes at 1.5 cm intervals are made on the side of the tank wall. The pressures sensors used in this study were piezoelectric transducers with a range of 2 psi and a frequency response of 10,000 Hz. The sensitivity of these sensors is of the order of 0.15 mV/psi. The sensors were specially fabricated with a silicon gel coating in order to remove the possibility of any *zero-shift* problems associated with the change of media the sensor comes in contact with. In the absence of such a layer, periodic artificial spikes due to the unbalancing of the bridge resistance are observed which contaminate measurements. The sensor performs this way due to the response of the bridge elements to the cooling effect of water. Although water is at room temperature, it cools the diaphragm due to its higher thermal conductivity (Souter and Krachman). Alternating exposure to air and water during sloshing causes this difficulty, which if not ameliorated can affect measurements significantly.

6.3 System Identification

Time-histories of the non-dimensional base shear force are plotted in Fig. 6.2 for A_e = 0.3 cm and 2.0 cm. As noted from the figure, the resonant condition occurs at different frequency ratios for the two cases, e.g., $\gamma_f = 1.10$ at A_e =0.3 cm and $\gamma_f = 1.20$ at A_e =2.0 cm. Sine-sweep studies were conducted in order to construct the frequency response curves.

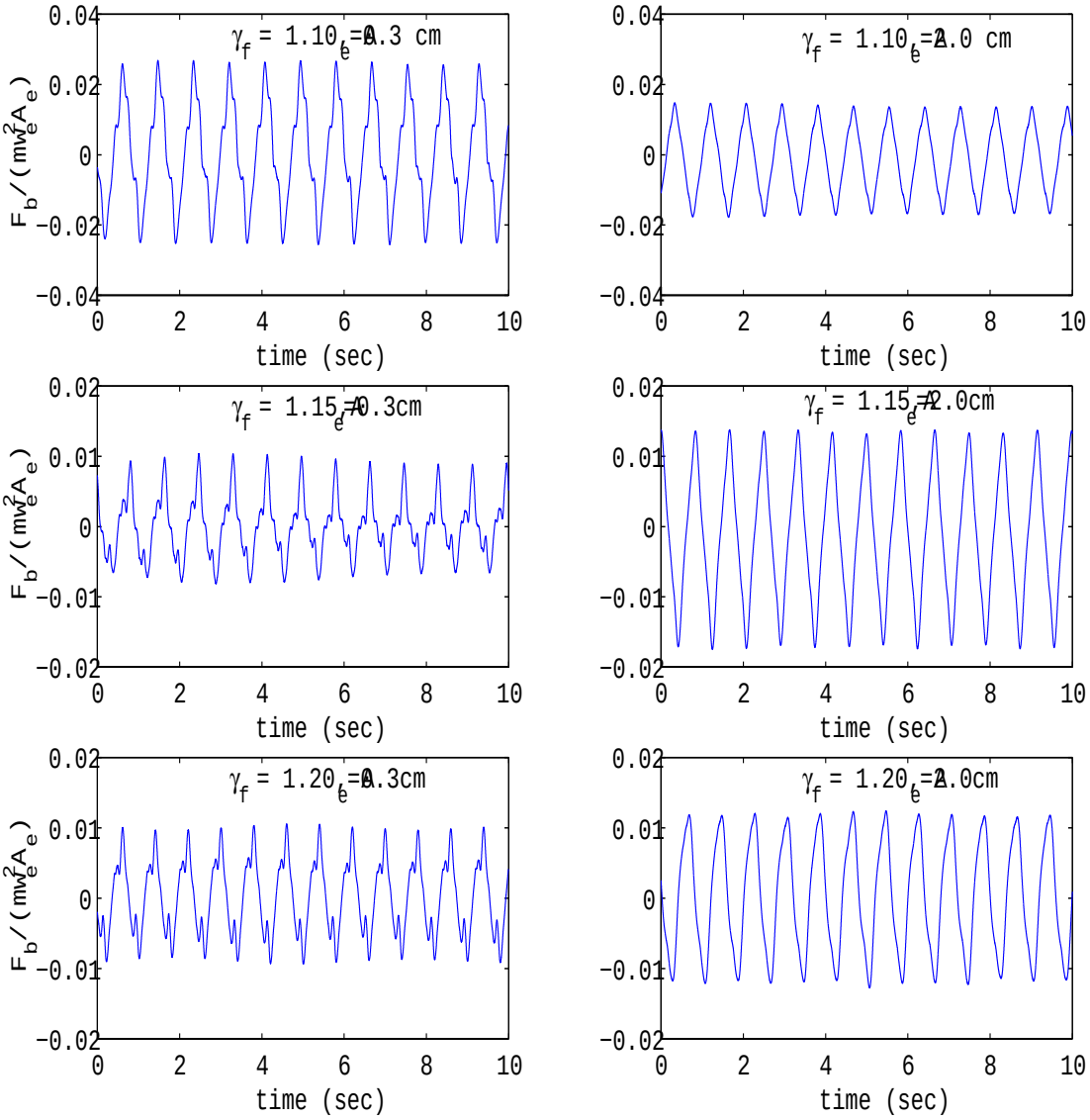

Figure 6.2 Sample time-histories of the shear force at A_e = 0.3 cm and 2.0 cm

6.3.1 Nonlinear System Identification

A nonlinear identification scheme was utilized to determine the parameters for the nonlinear impact characteristics of the TLD. The algorithm used was a nonlinear least squares constrained optimization algorithm in the MATLAB optimization toolbox (Grace 1992). The objective function evaluates the square of the error between the experimental

data and the simulated data using the assumed values of the unknown parameters. The flowchart of the optimization scheme is shown in Fig. 6.3. Figure 6.4 shows the variation in the impact characteristic function parameters, i.e., φ and ς, introduced in chapter 2, as a function of the non dimensional amplitude of excitation. After optimization, the following expressions were obtained:

$$\eta \approx 2 \quad ; \quad \varphi(A_e) \approx \frac{2.3}{(A_e/a)^{0.78}} \quad ; \varsigma(A_e) \approx 1.78(A_e/a)^{0.68} \tag{6.4}$$

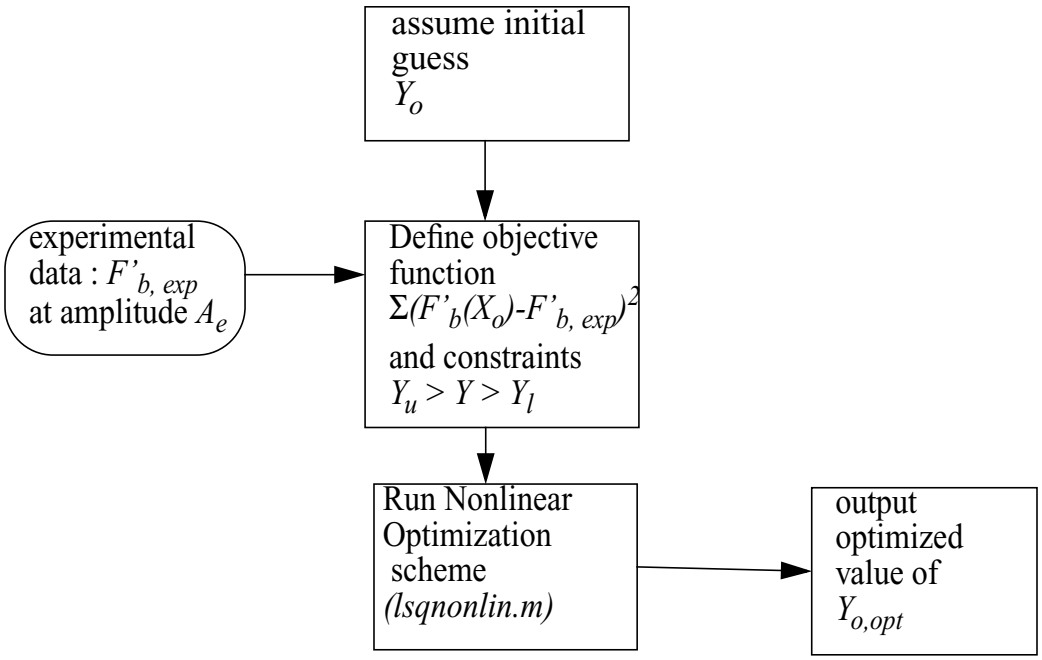

Figure 6.3 Nonlinear Optimization Scheme

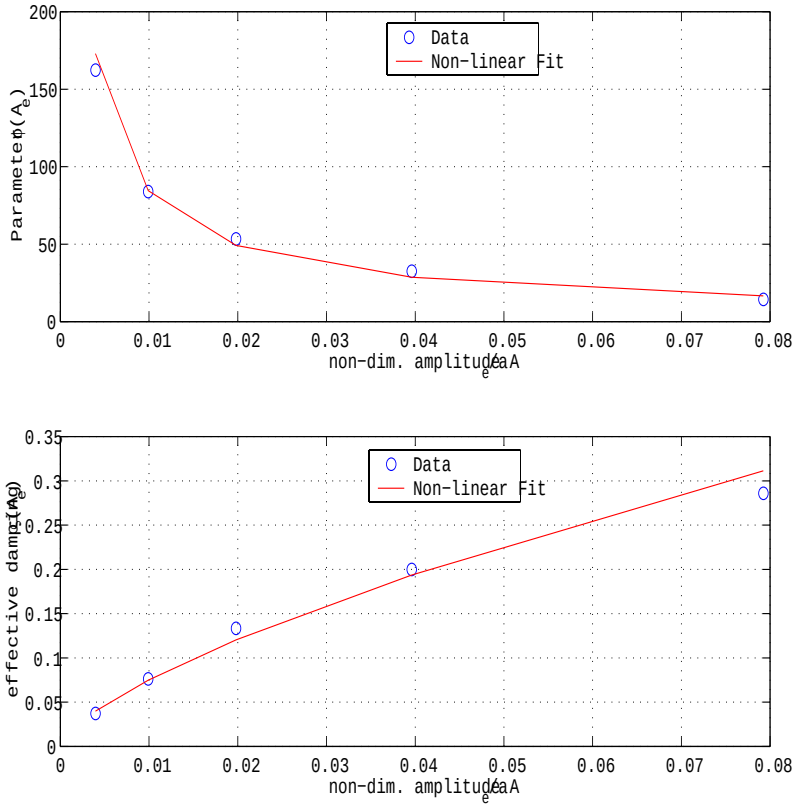

Figure 6.4 Curvefitting the parameters of the impact characteristics model

Equation 6.4 implies that the damping due to inherent liquid ($\zeta_f = 0.4\%$ calculated using Eq. 6.2) is negligible compared to the total damping, $(\varsigma(A_e))$, induced in the TLD due to sloshing at higher amplitudes. The results of the identification can be seen in Fig. 6.5 where the experimental non dimensional shear force and the analytical shear force plotted as a function of the frequency ratio are compared. The analytical model successfully captures the jump phenomenon and the widening of the frequency band very well. However, it was noticed that there is a presence of a sub-harmonic resonance at a frequency ratio of 0.96 which is not reflected by the nonlinear model. However, this resonance though present at low amplitudes is more pronounced at some medium amplitudes and is suppressed at high amplitudes. The current analytical model does not contain these

second-order effects. More complex models which include higher order nonlinearities can model this effect. However, this is not pursued in this study. Figure 6.5 suggests that even at low amplitudes (0.1 cm), the nonlinear jump phenomenon is present.

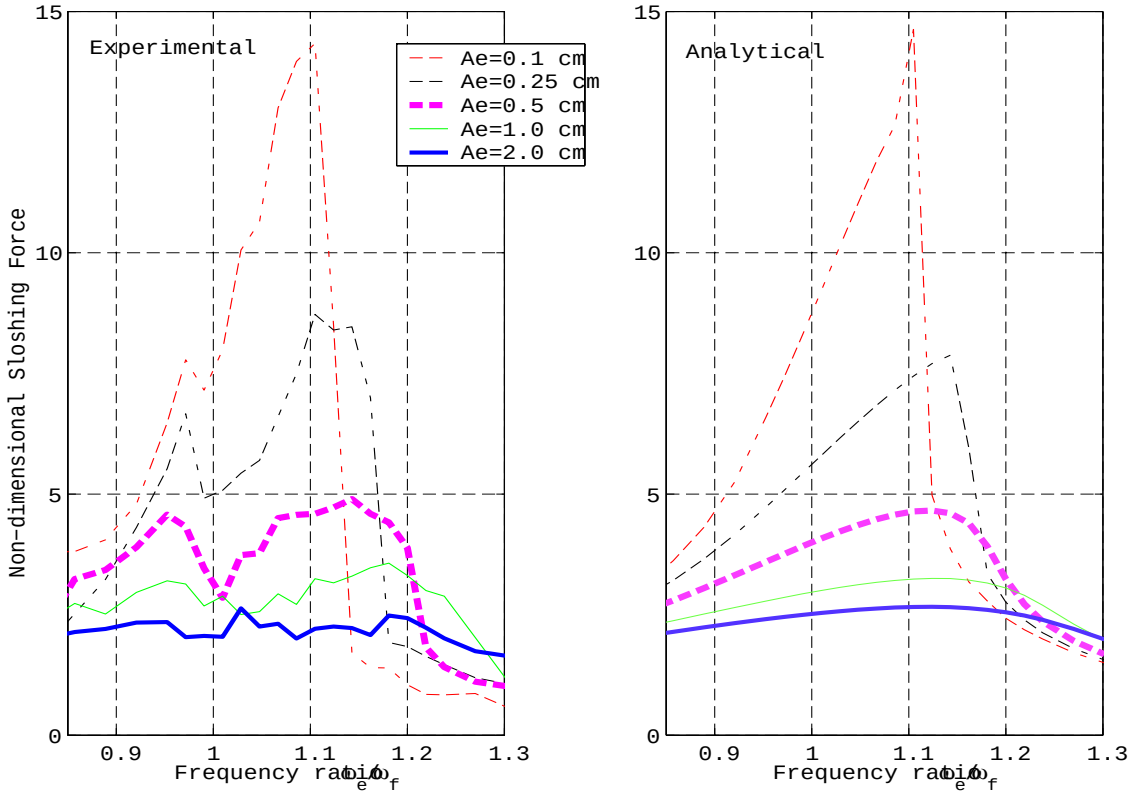

Figure 6.5 (a) Experimental plots of non-dimensional sloshing force as a function of excitation frequency for different amplitudes (b) Simulated curves after optimization

6.3.2 Combined Structure-damper analysis

Next, combined TLD-structure system is studied. The equations of motion of a structure represented as a SDOF system and TLD are given by,

$$M_s\ddot{X}_s + C_s\dot{X}_s + K_sX_s + c_f(\dot{X}_s - \dot{x}_f) + k_{eff}(X_s)X_s - k_{eff}(x_f)x_f = F_e(t) \qquad (6.5)$$

$$m_f\ddot{x}_f = c_f(\dot{X}_s - \dot{x}_f) + k_{eff}(X_s)X_s - k_{eff}(x_f)x_f \qquad (6.6)$$

where the subscripts s and f refer to the structure and damper respectively, and the rest of the symbols have been defined earlier. The mass ratio, $\mu = m_f/M_s$ is equal to 0.01 and

the tuning ratio $\gamma = \omega_f / \omega_s$ is equal to 0.99. Solving the equations of motion given in Eqs. 6.5 and 6.6 numerically and plotting the non-dimensional displacement of the structure (X_s/A_e) as a function of the frequency, the transfer functions as shown in Fig. 6.6 are obtained.

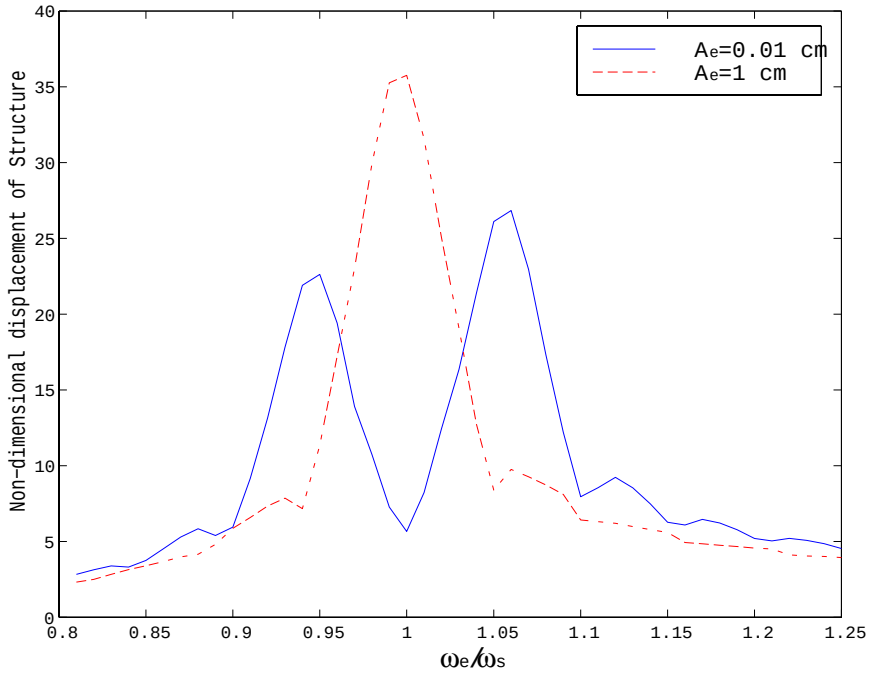

Figure 6.6 Response of the structure for different amplitudes

The combined TLD-structure system exhibits certain change in transfer function characteristics as the amplitude of excitation increases. The frequency response of a TLD, unlike a tuned mass damper, is excitation amplitude dependent. The increased damping (introduced by wave breaking and slamming) causes the frequency response function to change from a double-peak to a single-peak function like an over-damped TMD. This change in frequency response has also been observed experimentally, e.g., Sun and Fujino, 1994.

6.4 Impact Pressure Studies

The shallow water theory leads to a hydrostatic pressure description for loads on the sloshing container walls. This is appropriate when standing waves or small travelling waves are excited. However, as soon as impacts are recorded at the walls, the pressure distribution appears very different due to the presence of the impulsive peaks. At this time, the pressure distribution at the vertical walls is far from hydrostatic. In this section, the local pressures on the walls of the TLDs arising due to the sloshing impacts of the liquid are studied in detail.

Seven measurement taps were drilled in the side of the tank for pressure sensors at intervals of 1.5 cm (Fig. 6.1(b)). Sensor 1 is at 1.5 cm from the bottom of the tank, sensor 2 is at 3.0 cm (static liquid level) and so on. The sampling frequency of the data acquisition system was maintained at 1000 Hz. This was found to be adequate since the duration of the peak impact in the resonant pressure trace was found to be of the order of 15-20 milli-seconds. Data acquisition for each case was carried out for about 30 sec which corresponded roughly to 30 cycles of data. The average value of the peak pressure over N cycles is calculated as follows:

$$[P_{peak}] = \frac{\sum_{i=1}^{N} P_{i,\,peak}}{N} \tag{6.7}$$

The pressure peak coefficient at a certain height z on the vertical wall is defined as:

$$K_{Pz} = \frac{[P_{peak}]}{\rho g a} \tag{6.8}$$

6.4.1 Single-point pressure measurement

Figure 6.7 shows typical pressure traces at different frequency ratios including resonant and non-resonant cases, i.e., γ_f = 0.7, 1.1 and 2.0. As seen from the plots, the impact peak pulses are present only at the resonant condition. As we know from base shear results, this resonant condition does not occur at γ_f = 1.0, but at 1.1 due to the hardening nature of the sloshing phenomenon.

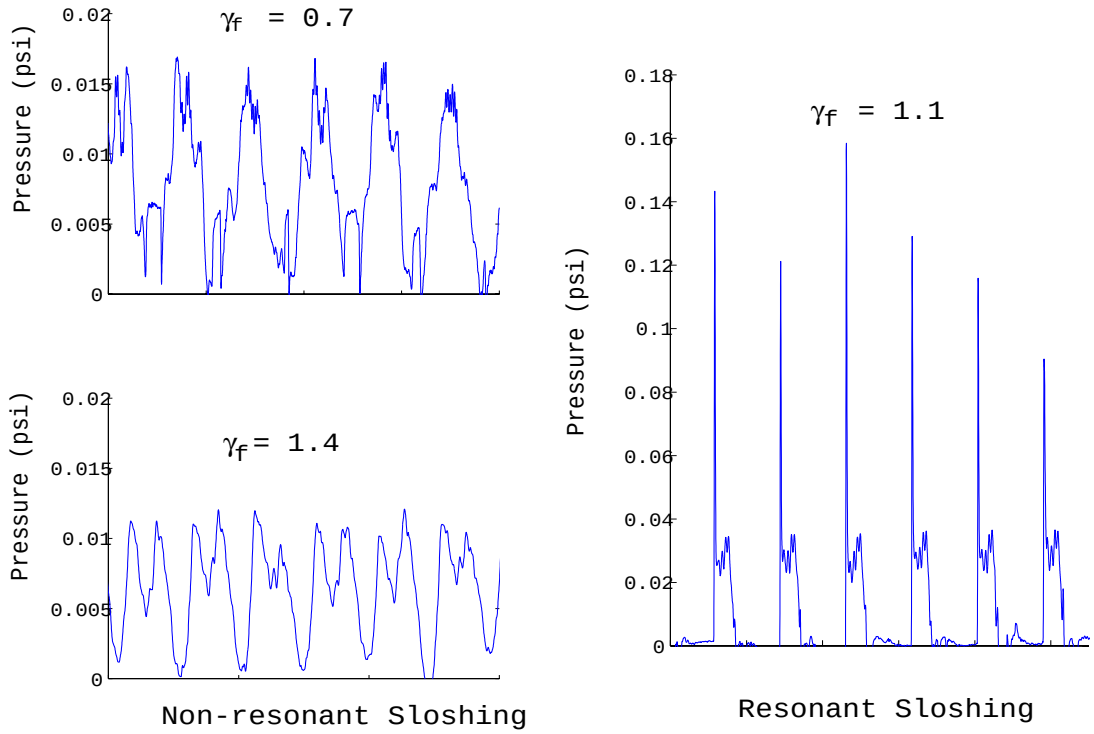

Figure 6.7 Pressure time histories for various frequency ratios (A_e = 1.0 cm).

It has been observed that these typical pressure time histories are neither harmonic nor periodic since the magnitude and duration of the peaks vary from cycle to cycle. This is true even though the excitation experienced by the tank is harmonic. Figure 6.8 shows the histogram of peak impact pressure for 100 cycles of pressure pulses for sensor at location 2. A statistical analysis of the pressure time records was conducted and the data was fitted with a *Lognormal* distribution (Fig. 6.8).

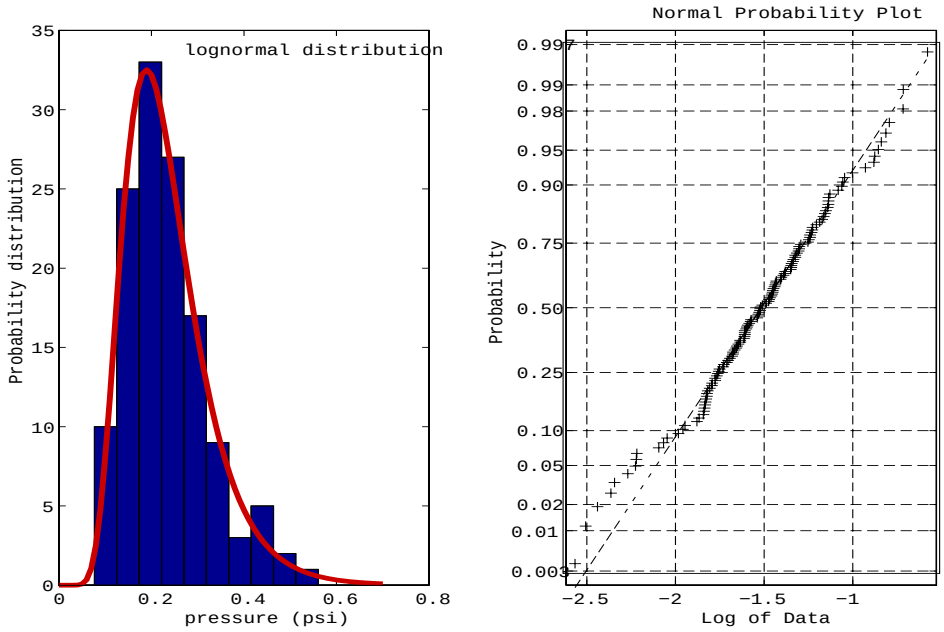

Figure 6.8 Probability distribution function of the peak impact pressures

Figure 6.9(a) shows the anatomy of a single pressure profile as it evolves over time along with corresponding visual photographs of wave sloshing. It is noteworthy that the impulsive peak is observed at 15 msec which suggests the high frequency slamming nature of the pressure pulse. After the initial impact caused by the wave, the full sloshing action of the wave is developed, which can be seen as a second peak of lower magnitude and longer duration. A wavelet *scalogram* (using *Morlet* wavelet) was utilized to study the time-frequency fluctuations of the pressure time-history. For more details on this technique, one can refer to Gurley and Kareem (1999). A scalogram is a plot wherein the square of the coefficients obtained by continuos wavelet transform (CWT) are plotted as a measure of the signal energy in the time-frequency domain. The scalogram of the pressure signal reveals the presence of high frequency components at the time of occurrence of the impulsive peak (Fig. 6.9b). The energy in regular sloshing is concentrated at lower frequencies which occurs after a certain time-lag following the initial impact.

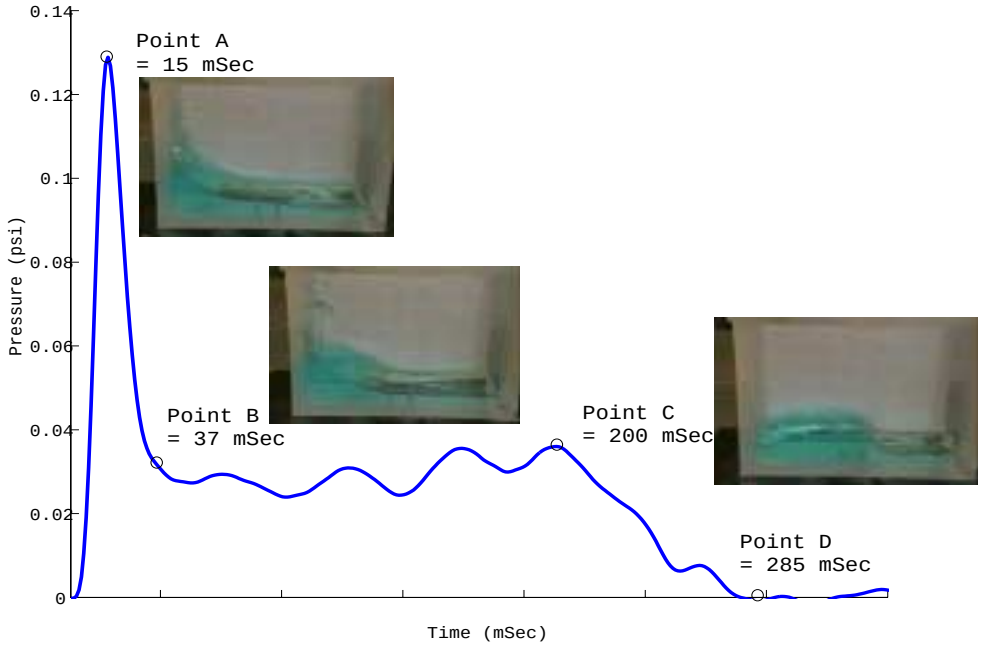

(a)

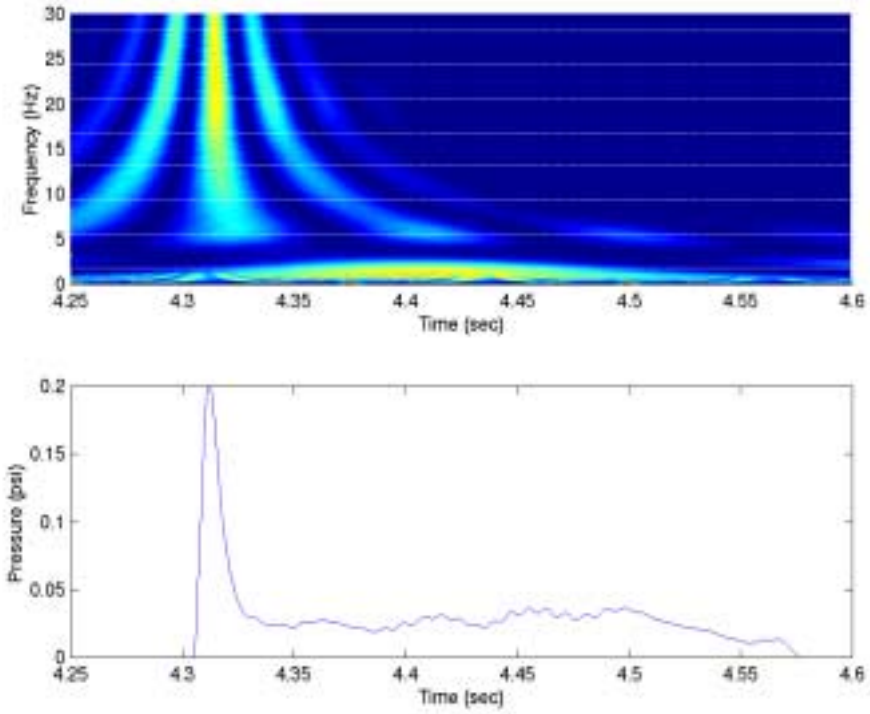

(b)

Figure 6.9 (a) Anatomy of a single pressure pulse (b) wavelet scalogram of the pressure signal

6.4.2 Multiple-point pressure measurements

Next, four sensors were recorded simultaneously to observe the time-lag as the pulse travels along the tank height and the spatial distribution of the impulsive peak to the overall slosh pulse. Figure 6.10 shows the simultaneous pressure pulse traces for a single cycle. The time-lag is measured with respect to sensor 2 (which is at the mean water level). The impact influence factor (*IIF*) is defined as:

$$IIF = \frac{A_i}{A_t} \tag{6.9}$$

where A_i is the area under the impulsive peak in the pressure time-history and A_t is the total area under the sloshing/slamming trace (including the impulse component). It is observed that at levels above the water level, the contribution is entirely due to impulsive slamming. On the other hand, the contribution of slamming at sensor 1, which is below the water level is only about 10%. This corroborates with topology of wave slamming because the slamming action is more prevalent in the region above the mean water level. The rolling convective mass of water, which is responsible for the slamming action, is primarily effective at these locations. The time-lag and *IIF* for the four locations are documented in Table 6.1.

Figure 6.10(b) shows the *coscalograms* of the different sensor measurements. A coscalogram in wavelet analysis is analogous to the cospectrum in the spectral analysis. Like the scalogram, it is useful in revealing time varying pockets of high and low correlation in different frequency bands. It is obtained by plotting the product of the wavelet coefficients of two signals as a function of time and frequency. The coscalograms in Fig. 6.10(b) are plotted with reference to sensor 2. The light patches in the coscalograms help identify areas of correlation. It is noted that the maximum correlation between each sen-

sors is near the low frequency sloshing component of the pressure signals. The correlations in the high frequency slamming portion is maximum in the sensor 2-1 coscalogram and drops off progressively in the 2-3 and 2-4 coscalograms due to the time lag of peaks which was discussed earlier.

A pressure-time integration of the pulses recorded at sensors 2 and 3, averaged over a number of measurements, yields that the contribution of the impulsive peak is around 20-30% of the total contribution of the pulse. This is a substantial contribution which is neglected by most numerical simulations. Moreover, the peak pressures obtained due to slamming are 5-10 times higher than those obtained from regular sloshing as observed earlier. The sloshing-slamming damper analogy, described in Chapter 2, also emphasizes the importance of estimating the effect of the liquid slamming on the overall system response. Similar concerns have been expressed in the study of impact loading of vertical structures in the offshore community, where the impact pressures were assumed to be not important and hence were not considered in the design. However, Schmidt *et al.* 1992 have demonstrated that this is an inadequate approach to design.

TABLE 6.1 Time lag and impact influence factor for different sensor locations

	Time lag of peaks with respect to sensor 2 (msec)	**Impact influence factor *IIF* (%)**
1st sensor	-2	10
2nd sensor	0	21
3rd sensor	14	30
4th sensor	42	85

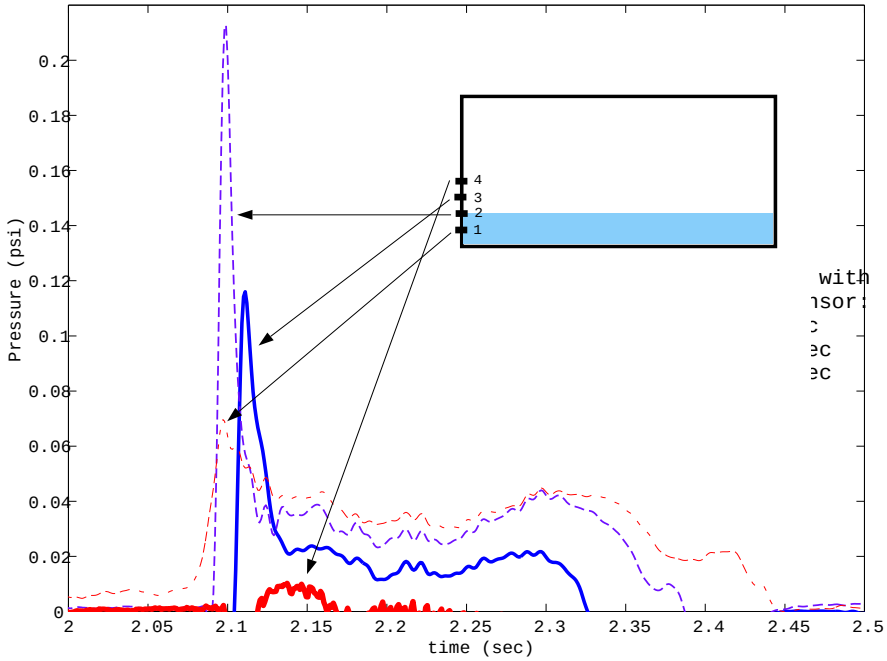

(a)

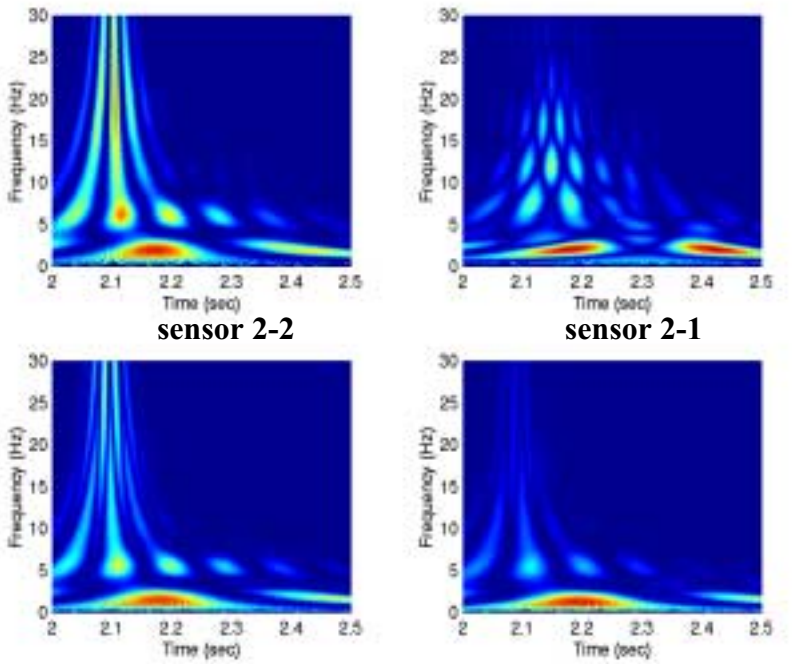

sensor 2-2 **sensor 2-1**

sensor 2-3 **sensor 2-4**

(b)

Figure 6.10 (a) Pressure pulses at different locations on the wall (b) Wavelet coscalograms with sensor 2 as reference

6.4.3 Shallow water *versus* deep water sloshing

Until now, the results presented were for the shallow water case ($h/a < 0.15$). In this case, sloshing at high amplitudes is characterized by travelling waves and hydraulic jumps (Fig. 6.11a). For deep water cases, i.e, $h/a > 0.15$, large standing waves are usually formed at resonance. Figure 6.11(b) shows the difference between the shallow water (h/a =0.12) slosh pressure trace and deep water (h/a = 0.25) pressure traces for the pressure tap locations at the mean water level. In the case of shallow water TLD, the pressure is maximum at the mean liquid level, while for the case of deep water TLD, impact pressures are also observed in a large part of the ceiling. The impulsive peak is more pronounced in the shallow water case and reaches peak value at 15 msec as opposed to the deep water case where the peak value is reached at 50 msec.

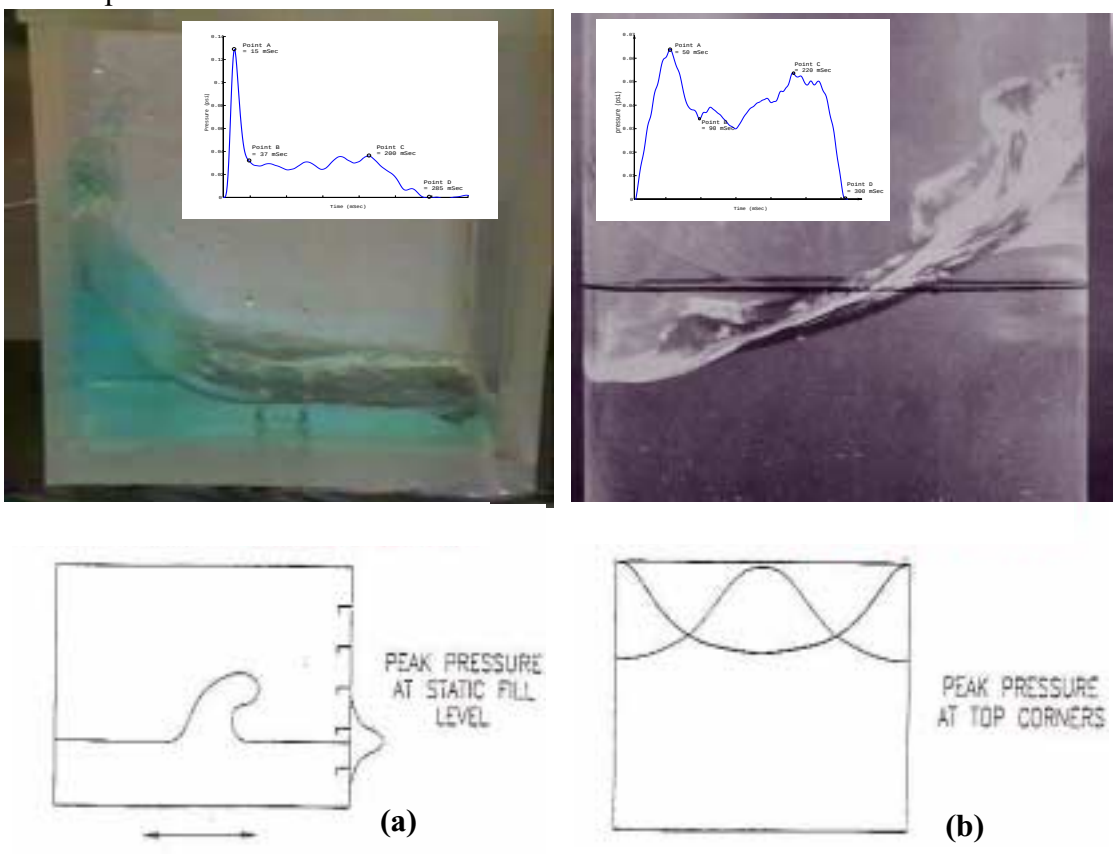

Figure 6.11 Typical sloshing wave with pressure pulse and wave mechanism schematic for (a) shallow water (h/a =0.12) and (b) deep water (h/a = 0.25) case

6.4.4 Pressure variation along the tank height

The pressure distribution over the tank walls is important for establishing integral load effects due to slamming and design considerations of walls under sloshing/slamming-induced loads. Bass *et al.* 1980 have provided an idealized distribution for vertical tank walls based on their experiments in terms of a pressure coefficient which was described by the following cosine function:

$$K_{Pz} = \frac{1}{2}K_{Pmax}\left[1 + \cos\left(\frac{5\pi(z-h)}{H}\right)\right]; \quad h - \frac{H}{5} \le z \le h + \frac{H}{5} \tag{6.10}$$

where K_{Pz} is the peak pressure coefficient, K_{Pmax} is the maximum pressure coefficient (which occurs at the mean water level for the shallow water case), z = distance from tank bottom, h = liquid filling height, H = tank height. As seen from Fig. 6.12, where the maximum pressure coefficients at A_e = 2.0 cm are plotted along the height of the wall. One can note that the curve described by Eq. 6.10 envelopes the maximum pressure peak coefficients obtained from the present studies.

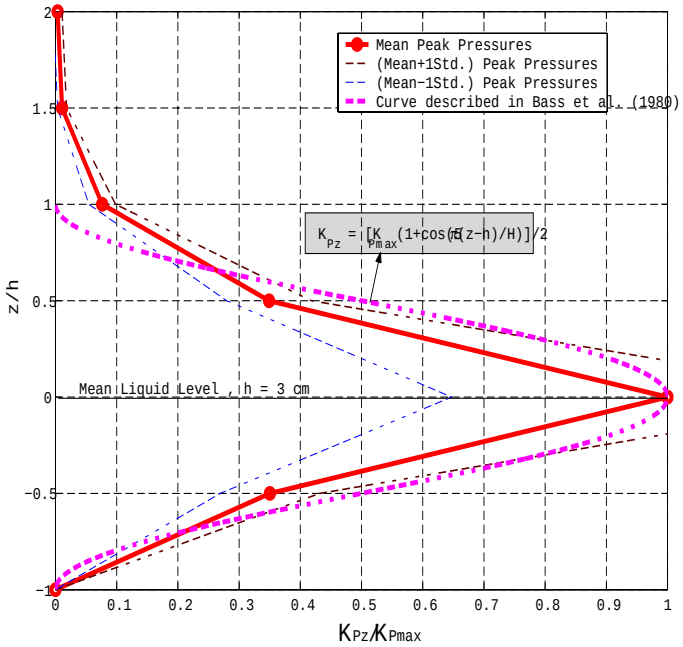

Figure 6.12 Variation of the peak pressure coefficient with height of the tank wall

6.5 Hardware-in-the-loop Simulation

One of the main areas of investigation in the design of TLDs is the actual performance when installed in a structure. Hardware-in-the-loop (HIL) refers to a simulation technique in which some of the system components are numerically simulated while others are physically modeled with appropriate interface conditions. Usually, there are real hardware characteristics that are unknown or too complex to model in pure simulations. In these situations, HIL is an extremely useful simulation technique. Hardware-in-the-loop developed out of a hybrid between *control prototyping* and software-in-the-loop simulations (Isermann, 1999). HIL is routinely used in aerospace, automotive control and embedded systems engineering as an inexpensive and reliable rapid-prototyping technique for product development. Its application in structural testing of damping systems has been rather limited.

This method is especially applicable to structure-damper experimental studies. One can specify the external loading and model the structure by appropriate equations, which are solved in real-time to obtain the displacement response. This displacement is used to drive the shaking-table on which the damper is mounted. The base-shear force due to sloshing liquid in the damper is simultaneously measured and feedback into the computer where it is used in the fore mentioned numerical equations. Thus, a real-time dynamic coupled structure-damper analysis is conducted without the use of an actual physical structure or heavy actuators to actuate the structure.

Some of the advantages of HIL simulation over conventional testing methods are the cost and time savings in repeated simulations. Figure 6.13 shows the difference in scale and the associated costs one can achieve with HIL testing for combined structure-damper experiments. The dynamic testing of structural systems with nonlinear append-

ages require considerable infrastructure involving structural system model, actuators, reaction wall system, and instrumentation. Often the actuators are limited in their dynamic capability which restricts these tests to a *pseudo*-dynamic level. While, in HIL simulation, one can build a *virtual structure* in a computer model and the non-linear structural elements, such as dampers, hysteretic elements and base-isolators, can be included in the physical structural model. Moreover, one needs a smaller shaking table for component testing. One of the most useful aspects of the HIL testing is that the user can perform *on-the-fly* tuning of important structural and excitation parameters. This can help in identifying important parametric relations between the two systems. A computer controlled system, which is standard in most dynamic testing laboratories and an essential component for implementing controllers for the shaking table, is needed to conduct the test in real-time. Some of the main issues for the success of this test is the speed of the computer control system. The disadvantage of the test is that a good system model is needed for the structure which is not available in all cases.

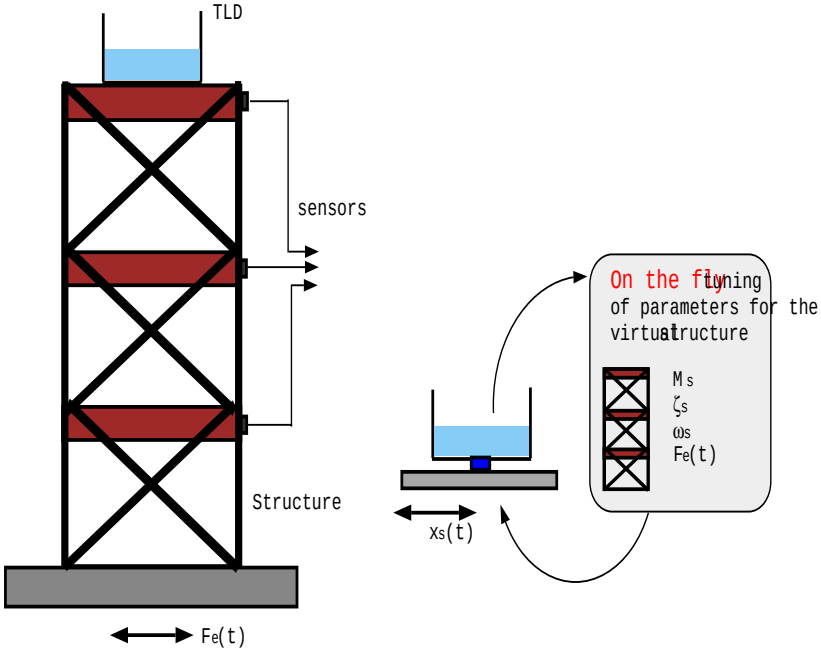

Figure 6.13 Hardware-in-the-loop concept for structure-liquid damper systems

6.5.1 Experimental study

Figure 6.14 shows a schematic of the experimental setup for verification of the hardware-in-the-loop concept. It is similar to the experimental setup shown in Fig. 6.1. As discussed earlier, the net sloshing force, $F_b(t)$, due to the liquid sloshing alone was obtained by subtracting the inertial contribution of the empty tank from the total shear force. For the combined structure-damper system, the equation of motion of the structure can be written as,

$$M_s\ddot{X}_s + C_s\dot{X}_s + K_sX_s = F_e(t) + F_b(t) \tag{6.11}$$

The displacement of the structure was calculated using the finite-difference version of Eq. 6.11 and the displacement signal was sent back as a voltage to the shaking table. In this way a real-time experiment of the combined dynamics of the structure and the damper was conducted.

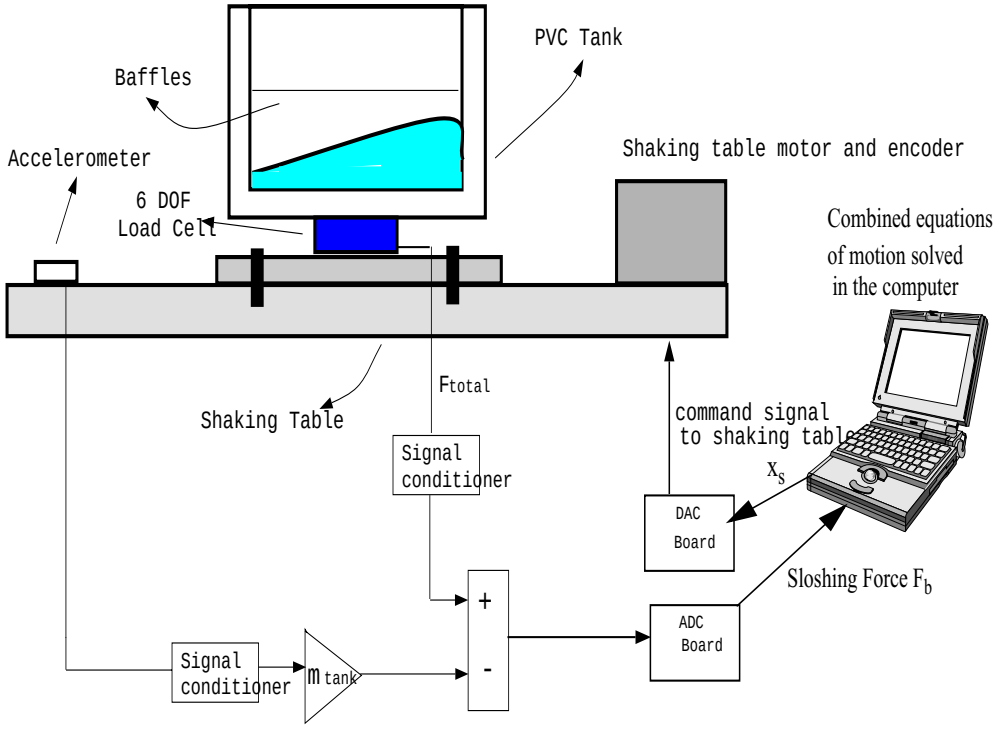

Figure 6.14 Schematic of the experimental setup for the HIL simulation

An important aspect of the HIL simulation is the real-time integration algorithm. For real-time simulation one should use fixed-time steps and should require inputs for derivative calculations that occur at the current time step and earlier. This means that fourth-order *Runge-Kutta* method is not applicable in such circumstances. Euler's first order algorithm has poor characteristics. The *Adams-Basforth* second order algorithm seems to provide much better accuracy yet it is suitable for real-time use. The displacement of the structure for the next time step t_{j+1} is calculated from displacements and velocities at current and earlier time steps t_j and t_{j-1} as,

$$X_{s,\,j+1} = X_{s,\,j} + \Delta t\left(\frac{3}{2}\dot{X}_{s,\,j} - \frac{1}{2}\dot{X}_{s,\,j-1}\right) \tag{6.12}$$

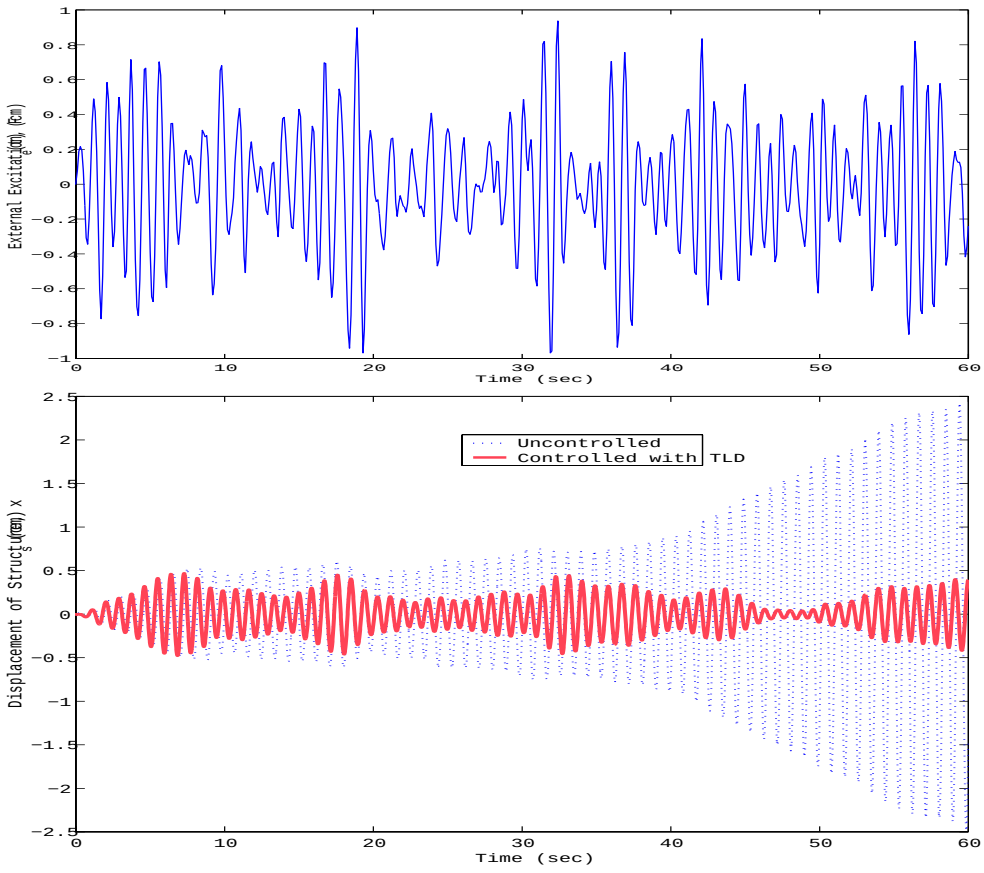

Figure 6.15 Hardware-in-the-loop simulation for random loading case

In the current experiment, a fixed time step of 0.005 (sampling frequency of 200 Hz) was utilized. This was suitable for our application as the frequency range of interest was less than 5 Hz. The parameters used in the simulation are ω_s=1.1 Hz, ζ_s = 3% and μ = 10%. Figure 6.15 shows the excitation time history used which is a random white noise signal. The figure also shows a comparison of the uncontrolled response and the controlled response by including the sloshing force due to the TLD. The total reduction in RMS response with and without the damper is 75%.

6.6 Concluding Remarks

A new sloshing model incorporating impact characteristics has been presented. The model parameters can be obtained from experimental data obtained by an instrumented sloshing tank placed on the shaking table. Impact pressure distributions were also measured along the height of the container. It was noted that the slamming action is present in shallow water TLDs and has a significant contribution to the overall sloshing force. These impact pressure studies also indicate the nature of sloshing-slamming along the height of the container, for e.g., at levels below the static liquid level, the pressure is dominated by the sloshing component while at levels above the static liquid level, it is governed by the slamming action. Finally, a new technique, namely the hardware-in-the-loop testing technique was presented for testing structure-liquid damper systems. This method promises to be a cheaper alternative to dynamic testing without the use of an actual structure, its scale model or large high-speed dynamic actuators to induce dynamic loading.